


Research Article

Mixed Convection and Thermally Radiative Flow of MHD Williamson Nanofluid with Arrhenius Activation Energy and Cattaneo–Christov Heat-Mass Flux

S. Eswaramoorthi ¹, Nazek Alessa ², M. Sangeethavaanee ¹, Safak Kayikci ³,
and Ngawang Namgyel ⁴

¹Department of Mathematics, Dr. N. G. P. Arts and Science College, Coimbatore, Tamil Nadu, India

²Department of Mathematical Sciences, Faculty of Science, Princess Nourah Bint Abdulrahman University, Riyadh, Saudi Arabia

³Department of Computer Engineering, Bolu Abant Izzet Baysal University, Bolu, Turkey

⁴Department of Humanities and Management, Jigme Namgyel Engineering College, Royal University of Bhutan, Dewathang, Bhutan

Correspondence should be addressed to S. Eswaramoorthi; eswaran.bharathiar@gmail.com and Ngawang Namgyel; ngawangnamgyel@jnec.edu.bt

Received 15 June 2021; Accepted 30 July 2021; Published 18 August 2021

Academic Editor: Riaz Ahmad

Copyright © 2021 S. Eswaramoorthi et al. This is an open access article distributed under the Creative Commons Attribution License, which permits unrestricted use, distribution, and reproduction in any medium, provided the original work is properly cited.

In this paper, we explored the impact of thermally radiative MHD flow of Williamson nanofluid over a stretchy plate. The flow in a stretchy plate is saturated via Darcy–Forchheimer relation. Cattaneo–Christov heat-mass flux theory is adopted to frame the energy and nanoparticle concentration equations. Additionally, the mass transfer analysis is made by activation energy and binary chemical reaction. Activation energy is invoked through the modified Arrhenius function. The intention of the current investigation is to enhance the heat transfer rate in industrial processes. The non-Newtonian nanofluids have more prominent thermal characteristics compared to ordinary working fluids. The governing models are altered into ODE models, and these models are numerically solved by applying the MATLAB `bvp4c` algorithm. The graphical and tabular interpretations have scrutinized the impact of sundry distinct parameters. The fluid speed escalates for enhancing the Richardson number, and it falls off for higher values of the Weissenberg number. It is noticed that the fluid temperature declines for higher values of the Brownian motion parameter and it grows for larger values of the thermophoresis parameter. The activation energy enriches the heat transfer gradient and suppresses the local Sherwood number. Additionally, the more significant heat transfer gradient occurs in heat-absorbing nonradiative viscous nanofluid and a smaller heat transfer gradient occurs in heat-generating radiative Williamson nanofluid. Also, we noticed that a higher heat transfer gradient appears in the Fourier model than in the Cattaneo–Christov model. In addition, the comparative results are confirmed and reached an outstanding accord.

1. Introduction

Cooling and heating procedures are essential in many industries, and fluids make this process. The effectual cooling techniques are essential for cooling a higher thermal system in a short time. However, ordinary fluids such as ethylene glycol, engine oil, and water have poor thermal conductivity and do not fulfill the demand for powerful heat transfer

cooling agents. Considering the needs of modern industry, including microelectronics, chemical production, and power generation plants, we need to establish a new type of fluids that will be efficient in cooling thermal systems. Nanofluid is a fluid consisting of nanoparticles (nanosized particles) such as oxides, nitrides, carbides, and metals stably and uniformly suspended in a base fluid. These fluids overcome the difficulty of the base fluids and act as an agent of efficient cooling.

The nanofluid flow on a stretchy sheet was reported by Khan and Pop [1]. They noticed that the fluid temperature grows when the quantity of thermophoresis parameter is greater. Kuznetsov and Nield [2] addressed the natural convective flow of nanofluid on a plate. They noted that the heat transfer rate becomes less in the presence of the Brownian motion parameter. Goyal and Bhargava [3] derived the numerical solution of viscoelastic nanofluid on a sheet under velocity slip condition. Their outcomes clearly show that the thermophoresis parameter leads to deceleration in the fluid temperature. The Titania nanofluid flow in a cylindrical annulus was illustrated by Mebarek-Oudina [4]. The problem of bioconvective flow of MHD tangent hyperbolic nanofluid subject to Newtonian heating was solved by Shafiq et al. [5]. They detected that the nanoparticle concentration suppresses when rising the thermophoresis parameter. Mabood et al. [6] illustrate the consequence of MHD flow of hybrid nanofluid on a wedge with thermal radiation. They proved that the fluid velocity uplifts when enriching the magnetic field parameter.

In nature, heat transference occurs due to the temperature difference between one body to another body or within the same body. In the past, the heat transfer phenomenon was mostly addressed by using “Fourier’s law of heat conduction.” However, this law is not sufficient to express the fundamental characteristic of heat transfer. That is, each part of the entire object having an initial disturbance. In general, there is no material satisfying this property. To overcome this complication, Cattaneo [7] incorporated the thermal relaxation in Fourier’s theory which implements the heat transport is identical to the propagation of thermal waves with normal speed. Christov [8] upgraded the Cattaneo model by recommending the thermal relaxation time with upper convected Oldroyd’s derivatives for the frame-invariant formation. The time-dependent flow of nanofluid with Cattaneo–Christov double diffusion was examined by Ahmad et al. [9]. They noticed that the thermal relaxation parameter declines the fluid temperature. Reddy and Kumar [10] delivered the impact of Cattaneo–Christov heat flux of micropolar fluid on carbon nanotubes. The 2D incompressible flow of heat-generating/-absorbing Oldroyd-B fluid with Cattaneo–Christov heat flux on an uneven stretching sheet was portrayed by Ibrahim and Gadisa [11]. They proved that the heat flux relaxation time parameter leads to thinning the thermal boundary layer thickness. Kumar et al. [12] analyzed the significance of Cattaneo–Christov flow on a cone. They detected that the smaller heat transfer gradient occurred in the wedge than the cone for varying the thermal relaxation time parameter. Some recent developments on this concept are collected in [13–19].

The convective fluid flows on a porous medium play a vital role in many science and engineering systems. Some examples are crude oil production, heat exchanger layouts, groundwater systems, grain amassing, nuclear waste disposal, warm insurance outlining, fossil fuels beds, and many others. Darcy developed a semiempirical equation that uses in low porosity and low-velocity conditions. These empirical equations were not sufficient for a larger

Reynolds number. In this situation, Forchheimer [20] was developed a new model named as the Darcy–Forchheimer model, which includes the square velocity term in the Darcian model. Pal and Mondal [21] derived the numerical solution of MHD fluid flow on Darcy–Forchheimer porous medium. They discovered that the mass transfer gradient accelerates for more availability of local inertia parameters. The dual solution of forced convective stagnation-point flow on a Darcy–Forchheimer porous medium over a shrinking sheet was derived by Bakar et al. [22]. They achieved that the fluid temperature declines in the first solution and enhances the second solution when raising the porosity parameter. Meraj et al. [23] inspected the Darcy–Forchheimer flow of Maxwell fluid with Cattaneo–Christov heat flux theory. They acknowledged that the thermal boundary layer thickness becomes high for a larger quantity of the porosity parameter. The Darcy–Forchheimer flow of H₂O-based CNTs on rotating disk was studied by Hayat et al. [24]. They found that the fluid velocity is a nonincreasing function of the porosity parameter. Latest improvements for these concepts are collected in [25–35].

In recent decades, many researchers are willing to study the chemical reactions and activation energy because they have more industrial applications. Few applications are fog formation, fibrous insulation, thermal oil recovery, cooling of nuclear reactors, etc. The mixed convective flow of Carreau nanofluid flow with activation energy was illustrated by Javed et al. [36]. Zaib et al. [37] explored the consequences of a binary chemical reaction and activation energy of a nonlinear radiative flow of Casson nanofluid on a Darcy–Brinkman porous medium. They detected that the thickening of the solutal boundary layer thickness when raising the activation energy parameter. The impact of activation energy of an electrically conducting Carreau nanofluid flow in a stagnation point was discussed by Hsiao [38]. Time-dependent MHD natural convective flow with Arrhenius activation energy was analyzed by Maleque [39]. He noticed that the activation energy is enhancing the nanofluid concentration. Mabood et al. [40] portray the outcomes of Arrhenius activation energy effect on micropolar fluid on a thin needle. They concluded that the Sherwood number decelerates for upsurging values of the activation energy parameter. The results of Arrhenius activation energy of a tangent hyperbolic fluid was revealed by Kumar et al. [41]. A variety of studies on this direction was found in [42–45].

The primary objective of this paper is to portray the 2D Darcy–Forchheimer radiative flow of Williamson nanofluid with subject to activation energy and heat absorption. The thermophoresis and Brownian motion effects are taking into account. The energy and mass equation models are constructed via Cattaneo–Christov heat-mass flux theory. The Darcy–Forchheimer flow of radiative Williamson nanofluid with activation energy and Cattaneo–Christov dual flux was not examined yet. So, we fill this gap and will give a significant contribution to the existing investigations. Generally, Williamson nanofluid has a wide range of usages in biological engineering; especially, it is used for computing

the heat and mass transmission through the vessels in blood and hemodialysis, see [46]. The impact of pertinent parameters of the governing model of velocity, temperature and nanofluid concentration, local skin friction, local Nusselt number, and local Sherwood number are examined in terms of tables, charts, and figures.

2. Mathematical Formulation

We exhibit the steady mixed convective flow of 2D Williamson nanofluid on a Darcy–Forchheimer porous medium over a stretchy sheet. Let x -axis is considered in the flow direction and y - is perpendicular to the flow. The uniform

magnetic effect B_0 is applied in the y -direction and the induced magnetic effect excluded becomes a small quantity of Reynolds number. The fluid temperature and nanofluid concentration nearby the boundary is T_w and C_w which is larger than the ambient fluid temperature T_∞ and concentration C_∞ , respectively. The Cattaneo–Christov model replaced Fourier’s heat conduction law. The consequences of activation energy and binary chemical reaction are considered for our study. In addition, the fluid is heat consumption/generating. Under the above considerations, the governing flow problems are (see [47])

$$\begin{aligned} \frac{\partial u}{\partial x} + \frac{\partial v}{\partial y} &= 0, \\ u \frac{\partial u}{\partial x} + v \frac{\partial u}{\partial y} &= \nu \frac{\partial^2 u}{\partial y^2} + \sqrt{2}\Gamma \nu \frac{\partial u}{\partial y} \frac{\partial^2 u}{\partial y^2} - \frac{\nu}{k_1} u - \frac{C_b}{x\sqrt{k_1}} u^2 - \frac{\sigma B_0^2 u}{\rho_f} + \frac{1}{\rho_f} [(1 - C_\infty)\rho_{f\infty}\beta(T - T_\infty) - (\rho_p - \rho_{f\infty})(C - C_\infty)]g, \\ u \frac{\partial T}{\partial x} + v \frac{\partial T}{\partial y} + \lambda_T \Omega_T &= \alpha \frac{\partial^2 T}{\partial y^2} + \frac{1}{\rho C_p} \frac{16\sigma^* T_\infty^3}{3k^*} \frac{\partial^2 T}{\partial y^2} + \frac{Q}{\rho_f C_p} (T - T_\infty) + \tau \left[D_B \frac{\partial T}{\partial y} \frac{\partial C}{\partial y} + \frac{D_T}{T_\infty} \left(\frac{\partial T}{\partial y} \right)^2 \right], \\ u \frac{\partial C}{\partial x} + v \frac{\partial C}{\partial y} + \lambda_C \Omega_C &= D_B \frac{\partial^2 C}{\partial y^2} + \frac{D_T}{T_\infty} \frac{\partial^2 T}{\partial y^2} - k_r^2 (C - C_\infty) \left(\frac{T}{T_\infty} \right)^n \exp\left(\frac{-E_a}{\kappa T}\right), \end{aligned} \tag{1}$$

where

$$\begin{aligned} \Omega_T &= u \frac{\partial u}{\partial x} \frac{\partial T}{\partial x} + v \frac{\partial v}{\partial y} \frac{\partial T}{\partial y} + u^2 \frac{\partial^2 T}{\partial x^2} + v^2 \frac{\partial^2 T}{\partial y^2} + 2uv \frac{\partial^2 T}{\partial x \partial y} + u \frac{\partial v}{\partial x} \frac{\partial T}{\partial y} + v \frac{\partial u}{\partial y} \frac{\partial T}{\partial x}, \\ \Omega_C &= u \frac{\partial u}{\partial x} \frac{\partial C}{\partial x} + v \frac{\partial v}{\partial y} \frac{\partial C}{\partial y} + u^2 \frac{\partial^2 C}{\partial x^2} + v^2 \frac{\partial^2 C}{\partial y^2} + 2uv \frac{\partial^2 C}{\partial x \partial y} + u \frac{\partial v}{\partial x} \frac{\partial C}{\partial y} + v \frac{\partial u}{\partial y} \frac{\partial C}{\partial x}. \end{aligned} \tag{2}$$

All symbols are defined in the nomenclature part.

With the boundary conditions,

$$\text{at } y = 0: u = U_w(x) = ax, v = -V_w, T = T_w, D_B \frac{\partial C}{\partial y} + \frac{D_T}{T_\infty} \frac{\partial T}{\partial y} = 0, \tag{3}$$

$$\text{as } y \rightarrow \infty: u \rightarrow 0, T \rightarrow T_\infty, C \rightarrow C_\infty.$$

Define

$$\begin{aligned}\Psi &= y\sqrt{\frac{a}{\nu}}, \\ u &= xa f'(\Psi), \\ v &= -\sqrt{va} f(\Psi), \\ \theta(\Psi) &= \frac{T - T_\infty}{T_w - T_\infty}, \\ \phi(\Psi) &= \frac{C - C_\infty}{C_\infty}.\end{aligned}\tag{4}$$

The corresponding ODE's are

$$f''' - f'^2 + f f'' + We f'' f''' - \lambda f' - Fr f'^2 - M f' + Ri(\theta - Nr\phi) = 0,\tag{5}$$

$$\frac{1}{Pr}\left(1 + \frac{4}{3}R\right)\theta'' + f\theta' - \Gamma_T(f f'\theta' + f^2\theta'') + Hg\theta + Nb\theta'\phi' + Nt\theta'^2 = 0,\tag{6}$$

$$\frac{1}{Sc}\phi'' + f\phi' - \Gamma_C(f f'\phi' + f^2\phi'') + \frac{1}{Sc}\left(\frac{Nt}{Nb}\right)\theta'' - \sigma^{**}(1 + \delta\theta)^n \phi \exp\left(\frac{-E}{1 + \delta\theta}\right) = 0.\tag{7}$$

All parameters are defined in the nomenclature part.

The corresponding boundary conditions are

$$\begin{aligned}\text{At } \Psi = 0: & f(\Psi) = fw, f'(\Psi) = 1, \theta(\Psi) = 1, Nb\theta'(\Psi) + Nt\theta'(\Psi) = 0, \\ \text{As } \Psi \rightarrow \infty: & f'(\Psi) \rightarrow 0, \theta(\Psi) \rightarrow 0, \phi(\Psi) \rightarrow 0.\end{aligned}\tag{8}$$

The dimensionless form of wall shear stress, heat, and mass flux are expressed as

$$\begin{aligned}\frac{1}{2Cf\sqrt{Re}} &= f''(0) + \frac{We}{2}f''(0)^2, \\ \frac{Nu}{\sqrt{Re}} &= -\left(1 + \frac{4}{3}R\right)\theta'(0), \\ \frac{Sh}{\sqrt{Re}} &= \frac{Nb}{Nt}\theta'(0).\end{aligned}\tag{9}$$

3. Numerical Solutions

The ODE models (5)–(7) with associative conditions (8) are numerically solved by implementing MATLAB bvp4c

procedure. In this regard, first, we change the 2nd and 3rd order ODE into a system of first-order ODE.

Let $f = y_1$, $f' = y_2$, $f'' = y_3$, $\theta = y_4$, $\theta' = y_5$, $\phi = y_6$, and $\phi' = y_7$.

The system of first-order ODEs is as follows:

$$\begin{aligned}
 y_1' &= y_2, \\
 y_2' &= y_3, \\
 y_3' &= \frac{y_2^2 - y_1 y_3 + \lambda y_2 + Fr y_2^2 + M y_2 - Ri[y_4 - Nr y_6]}{1 + We y_3}, \\
 y_4' &= y_5, \\
 y_5' &= \frac{-y_1 y_5 + \Gamma_T y_1 y_2 y_5 - Hg y_4 - Nb y_5 y_7 - Nt y_5^2}{1/Pr(1 + 4/3R) - \Gamma_T y_1^2}, \\
 y_6' &= y_7, \\
 y_7' &= \frac{-y_1 y_7 + \Gamma_C y_1 y_2 y_7 - (1/Sc)(Nt/Nb)((-y_1 y_5 + \Gamma_T y_1 y_2 y_5 - Hg y_4 - Nb y_5 y_7 - Nt y_5^2)/(1/Pr(1 + 4/3R) - \Gamma_T y_1^2)) + \sigma^{**}(1 + \delta y_4)^n y_6 \exp(-E/1 + \delta y_4)}{1/Sc - \Gamma_C y_1^2},
 \end{aligned} \tag{10}$$

under the boundary conditions,

$$\begin{aligned}
 y_1(0) &= fw, \\
 y_2(0) - 1 &= 0, \\
 y_2(\infty) &= 0, \\
 y_4(0) - 1 &= 0, \\
 y_4(\infty) &= 0, \\
 Nb y_7(0) + Nt y_5(0) &= 0, \\
 y_6(\infty) &= 0.
 \end{aligned} \tag{11}$$

The numerical procedure needs initial calculation with tolerance 10^{-6} .

4. Results and Discussion

This section scrutinises the consequences of pertinent parameters on velocity, temperature, nanofluid concentration, skin friction coefficient, local Nusselt number, and local Sherwood number with a fixed quantity of Prandtl and Schmidt numbers. Table 1 provides the comparison of our numerical results and Mustafa et al. [47] results. We achieved that our results are exactly matched with Mustafa's results. The estimation of We , λ , Fr , M , Ri , and Nr on skin friction coefficient, local Nusselt number, and local Sherwood number was presented in Table 2. We noticed that the surface shear stress accelerates when enhancing the We and Ri values, and it decelerates for heightening the quantity of λ , Fr , M , and Nr values. The heat transfer gradient grows when growing the values of Ri , and it diminishes when upgrading the We , λ , Fr , M , and Nr values. Quite the opposite results are attained in the local Sherwood number. Table 3 describes the impact of Hg , R , Γ_T , Nb , and Nt on local Nusselt number. It is detected that the heat transfer gradient upturns when upturning the values of R , Γ_T , and Nb . On the contrary, it decimates for enhancing the quantity of

Hg and Nt . The variations of local Sherwood number for different values of σ^{**} , E , n , Γ_C , Nb , Nt , and δ were illustrated in Table 4. We found that the mass transfer gradients decelerate for the small quantity of σ^{**} , and after that, it enriches for higher magnitudes. The LSN develops when developing the values of n , Nb , and δ , and the opposite trend was obtained for the more presence of E , Γ_C , and Nt .

Figures 1(a) and 1(b) explain the impact of We and M on DFF and NDFD in velocity profile. We found that the fluid velocity decelerates for rising the values of We and M . Physically, a higher Weissenberg number leads to enriching the fluid relaxation time, and this causes to slow down the motion of the fluid particles. The higher magnitude of the magnetic field parameter develops the fluid resistance and this causes to suppress the motion of the fluid particles. Also, we have seen that higher momentum boundary layer thickness occurs in NDFD compared to the DFF. The changes of fluid velocity for diverse values of λ and Fr on WNF and VNF were presented in Figures 2(a) and 2(b). We noticed that the fluid velocity reduces when enriching the λ and Fr values. The thickness of the momentum boundary layer is lessened in WNF compared to VNF. Figures 3(a) and 3(b) show the variations of velocity profile for disparate values of fw and Ri . We achieved that the fluid velocity declines when escalating the fw values, and it grows when increasing the Ri values. Also, we have seen that the higher momentum boundary layer thickness occurs in NDFD compared to the DFF. The temperature distribution for diverse quantity of fw and Hg was illustrated in Figures 4(a) and 4(b). We detected that the fluid temperature diminishes when heightening the fw values and upturns for developing the Hg values. The larger values of the heat generation parameter enhance the fluid thermal state and this leads to enhance the fluid temperature. The thicken boundary layer occurs in DFF and radiation compared to NDFD and without radiation, respectively. Figures 5(a) and 5(b) depict the Nt and Nb consequences of temperature distribution.

TABLE 1: Comparison of local Nusselt number when $We = \lambda = Fr = R = \Gamma_T = Hg = \Gamma_C = 0$, $M = Nr = 0.5$, $Sc = 5$, and $\delta = 1$ by Mustafa et al. [47].

Pr	Nt	E	σ^{**}	n	Ri	Nu/\sqrt{Re}	
						[47]	Present
2.0	0.5	1.0	1.0	0.5	0.5	0.706605	0.706604
4.0						0.935952	0.935955
7.0						1.132787	1.132788
10.0						1.257476	1.257482
5.0	0.1	1.0	1.0	0.5	0.5	1.426267	1.426269
	0.5					1.013939	1.013938
	0.7					0.846943	0.846928
	1.0					0.649940	0.649939
5.0	0.5	0.0	1.0	0.5	0.5	0.941201	0.941209
		1.0				1.013939	1.013943
		2.0				1.064551	1.064563
		4.0				1.114549	1.114191
5.0	0.5	1.0	0.0	0.5	0.5	1.145304	1.145301
			1.0			1.013939	1.013938
			2.0			0.926282	0.926281
			5.0			0.798671	0.798669
5.0	0.5	1.0	2.0	-1.0	0.5	1.030805	1.030804
			-0.5			0.999470	0.999468
			0.0			0.964286	0.964285
			1.0			0.886830	0.886830
10.0	0.5	1.0	2.0	0.5	0.0	1.032281	1.032280
					0.5	1.056704	1.056706
					3.0	1.154539	1.154538
					5.0	1.215937	1.215938

TABLE 2: Numerically obtained values of skin friction coefficient, local Nusselt number, and local Sherwood number for various values of We , λ , Fr , M , Ri , and Nr .

We	λ	Fr	M	Ri	Nr	$1/2Cf\sqrt{Re}$	Nu/\sqrt{Re}	Sh/\sqrt{Re}
0.0	0.2	0.4	0.5	0.6	0.5	-1.369910	1.736070	-1.041642
0.1						-1.336353	1.731626	-1.038976
0.2						-1.299006	1.726528	-1.035917
0.3						-1.255948	1.720440	-1.032264
0.2	0.0	0.4	0.5	0.6	0.5	-1.150084	1.740831	-1.044499
	0.3					-1.332147	1.722392	-1.033435
	0.6					-1.426504	1.710895	-1.026537
	1.0					-1.542193	1.697346	-1.018407
0.2	0.2	0.0	0.5	0.6	0.5	-1.209294	1.733884	-1.040331
		0.4				-1.299007	1.726528	-1.035917
		0.8				-1.382682	1.719806	-1.031884
		1.2				-1.461128	1.713616	-1.028170
0.2	0.2	0.4	0.0	0.6	0.5	-1.035442	1.763066	-1.057839
			0.6			-1.332153	1.722392	-1.033435
			1.4			-1.569535	1.694225	-1.016535
			2.0			-1.722549	1.677325	-1.006395
0.2	0.2	0.4	0.5	0.0	0.5	-1.523325	1.699901	-1.019940
				0.4		-1.372881	1.718112	-1.030867
				0.7		-1.262365	1.730588	-1.038353
				1.0		-1.151000	1.743301	-1.045981
0.2	0.2	0.4	0.5	0.6	0.0	-1.289661	1.733515	-1.040109
				0.3		-1.295106	1.729398	-1.037639
				0.7		-1.303165	1.723548	-1.034129
				1.0		-1.309932	1.718840	-1.031304

TABLE 3: Numerically obtained values of local Nusselt number for the various values of Hg , R , Γ_T , Nb , and Nt .

Hg	R	Γ_T	Nb	Nt	Nu/\sqrt{Re}
-0.5	0.5	0.1	0.5	0.5	1.726528
-0.3					1.542341
0.0					1.205077
0.3					0.871873
0.5					0.349241
-0.5	0.0	0.1	0.5	0.5	1.438110
	0.3				1.619396
	0.6				1.776956
	1.0				1.962378
-0.5	0.5	0.0	0.5	0.5	1.701132
		0.1			1.726528
		0.2			1.753300
		0.3			1.775803
-0.5	0.5	0.1	0.5	0.5	1.726528
			1.0		1.730099
			1.5		1.731254
			2.0		1.731825
-0.5	0.5	0.1	0.5	0.0	1.833704
				0.5	1.726528
				1.0	1.627784
				1.5	1.537369

TABLE 4: Numerically obtained values of the local Sherwood number for various values of σ^{**} , E , n , Γ_C , Nb , Nt , and δ .

σ^{**}	E	n	Γ_C	Nb	Nt	δ	$Sh\sqrt{Re}$
0.0	1.0	0.5	0.1	0.5	0.5	1.0	-1.031660
0.7							-1.034681
1.3							-1.031771
2.0							-1.027447
1.0	0.0	0.5	0.1	0.5	0.5	1.0	-1.028634
	1.0						-1.033423
	2.0						-1.034617
	3.0						-1.033993
1.0	1.0	-1.0	0.1	0.5	0.5	1.0	-1.036196
		-0.5					-1.035629
		0.0					-1.034736
		0.5					-1.033423
		1.0					-1.026188
1.0	1.0	0.5	0.0	0.5	0.5	1.0	-0.776036
			0.1				-1.033423
			0.2				-1.053241
			0.3				-1.029591
1.0	1.0	0.5	0.1	0.5	0.5	1.0	-1.033423
				1.0			-0.517626
				1.5			-0.345282
				2.0			-0.259035
1.0	1.0	0.5	0.1	0.5	0.1	1.0	-0.216786
					0.5		-1.033423
					1.0		-1.949590
					1.5		-2.763326
1.0	1.0	0.5	0.1	0.5	0.5	0.0	-1.035867
						1.0	-1.033423
						2.0	-1.031309
						3.0	-1.029459

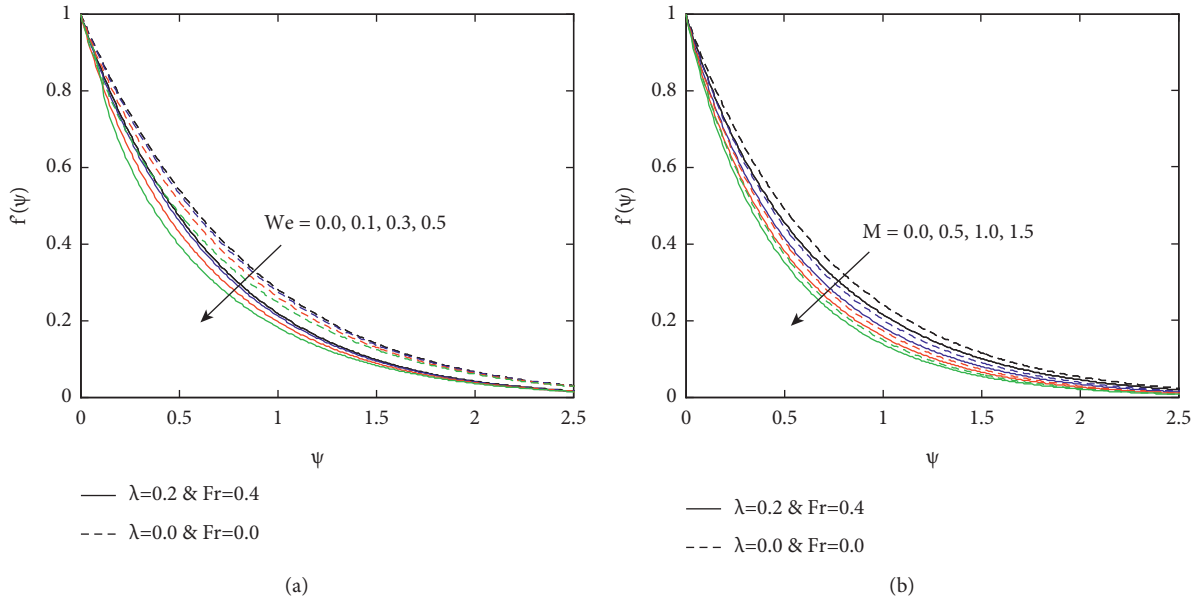


FIGURE 1: The velocity distribution for diverse quantity of We (a) and M (b).

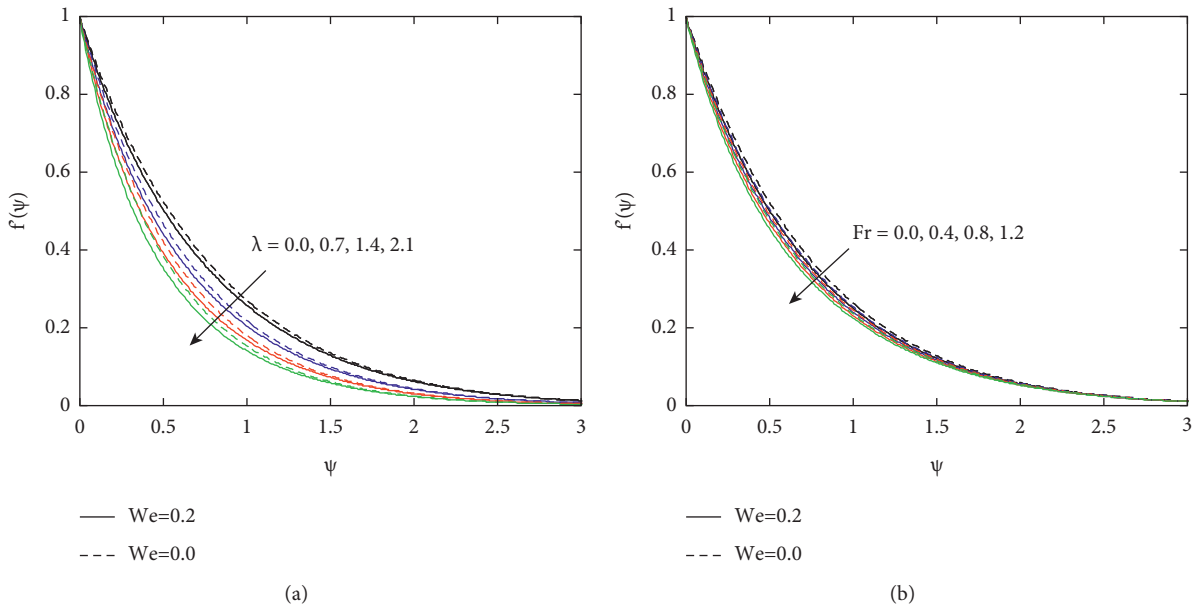


FIGURE 2: The velocity distribution for diverse quantity of λ (a) and Fr (b).

We exposed that the fluid temperature develops for increasing the Nt values and the opposite trend was obtained for Nb values. Also, we noticed that the reaction rate leads to suppressing of the thermal boundary layer thickness. The effects of Hg and R on temperature distribution were plotted in Figures 6(a) and 6(b). We noted that the fluid temperature raises for rising the Hg and R values. In addition, we found the larger thermal boundary layer thickness attains in the FHF model compared to the CCHF model. Figures 7(a) and 7(b) portray the consequences of fw and Nt for nanofluid

concentration profile. We concluded that the nanofluid concentration enhances near the plate and falling-off away from the plate. The Nt values lead to enriching the nanofluid concentration boundary layer thickness. The nanofluid concentration distribution for different values of Nb and Γ_C were shown in Figures 8(a) and 8(b). These figures clearly show that the nanofluid concentration is an increasing behavior for Γ_C and quite the opposite occurs for Nb values. Also, we noticed that the reaction rate leads to suppressing of the nanofluid concentration boundary layer thickness.

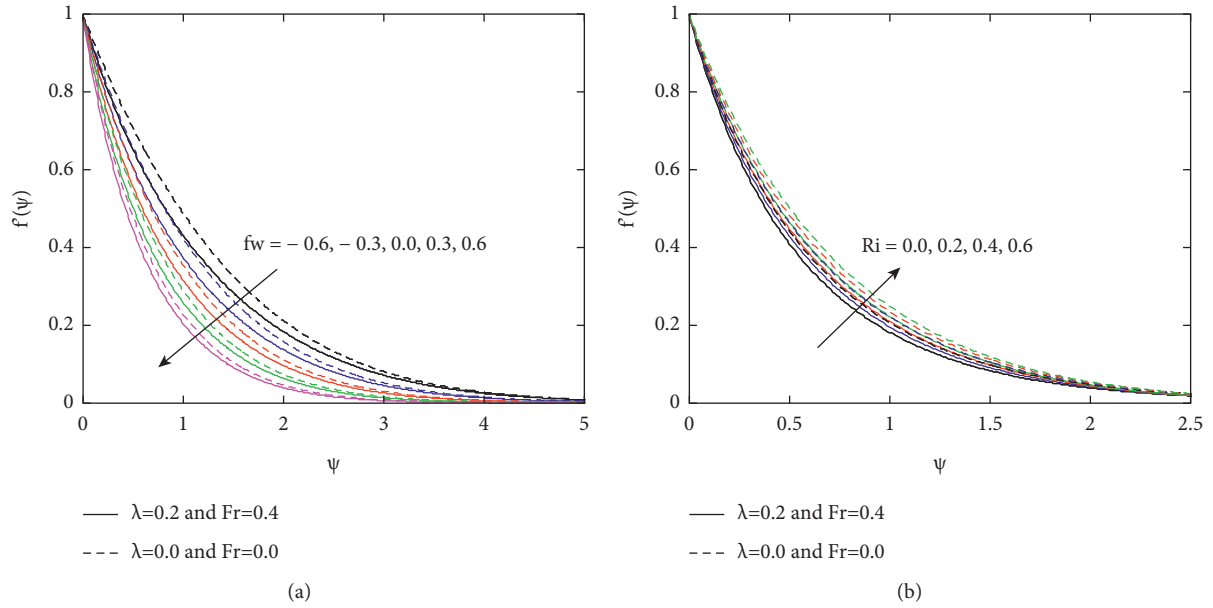


FIGURE 3: The velocity distribution for diverse quantity of fw (a) and Ri (b).

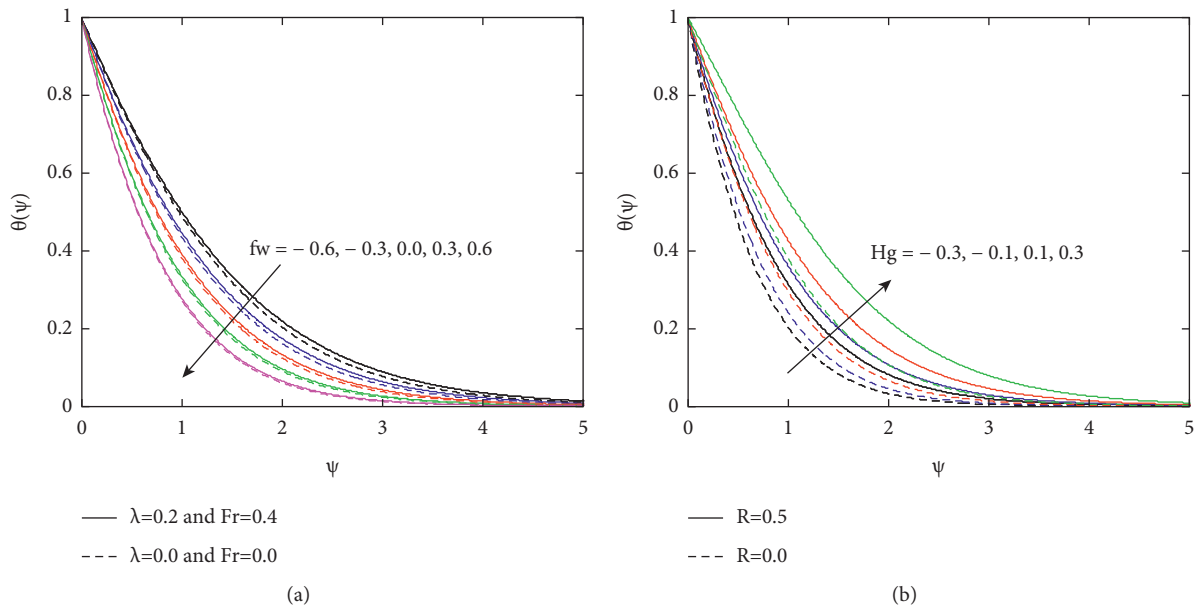


FIGURE 4: The temperature distribution for diverse quantity of fw (a) and Hg (b).

The skin friction coefficient on WNF and VNF on DFPM and NDFPM with $fw = -0.4$ and $fw = 0.4$ was plotted in Figures 9(a) and 9(b). We proved that the larger surface shear stress (-0.707201) occur in NDF of WNF with injection case and smaller surface shear stress (-1.36991) occur in DFF of VNF with the suction case. Figures 10(a) and 10(b) provide the skin friction coefficient on WNF and VNF on a DFPM and NDFPM with $Ri = 0.0$ and $Ri = 1.0$. We concluded that the larger surface shear stress (-0.875878) occur in the DFF of WNF with

the presence of Ri and smaller surface shear stress (-1.61002) occur in the DFF of VNF with the absence of Ri . The local Nusselt number on WNF and VNF with $R = 0.0$, $R = 1.0$, $Hg = -0.4$, and $Hg = 0.4$ with the CC model and the FF model was plotted in Figures 11(a) and 11(b) and Figures 12(a) and 12(b). In the CC model, the larger heat transfer gradient (1.97227) occurs in heat-absorbing radiative viscous nanofluid, and a smaller heat transfer gradient (0.718399) occurs in a heat-generating radiative viscous nanofluid. In the FF model, the larger

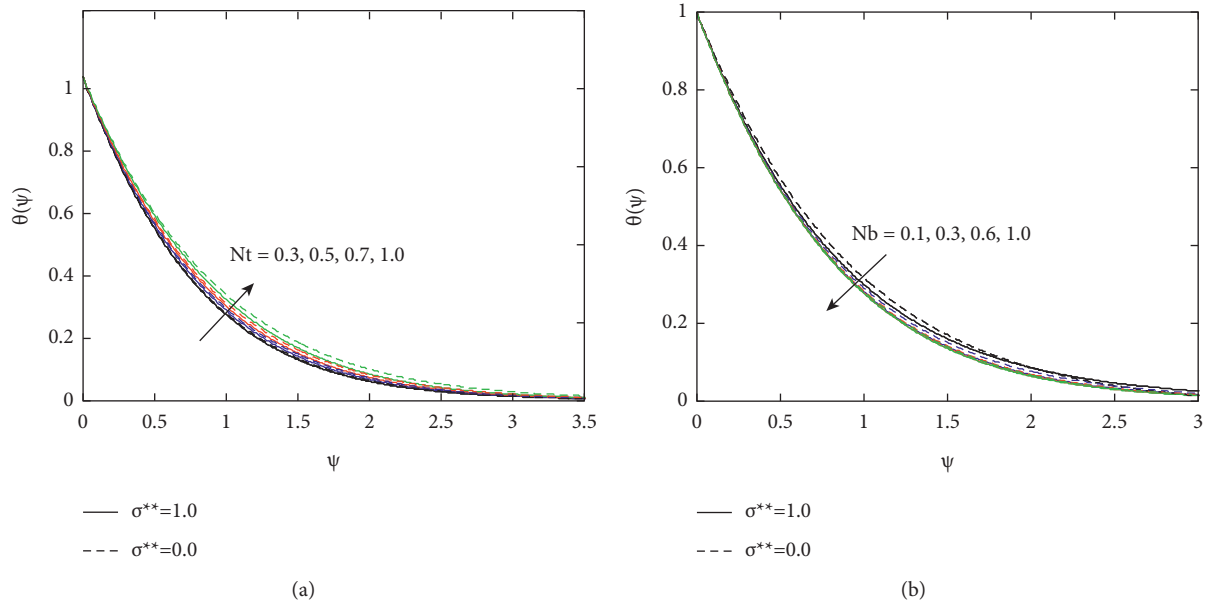


FIGURE 5: The temperature distribution for diverse quantity of Nt (a) and Nb (b).

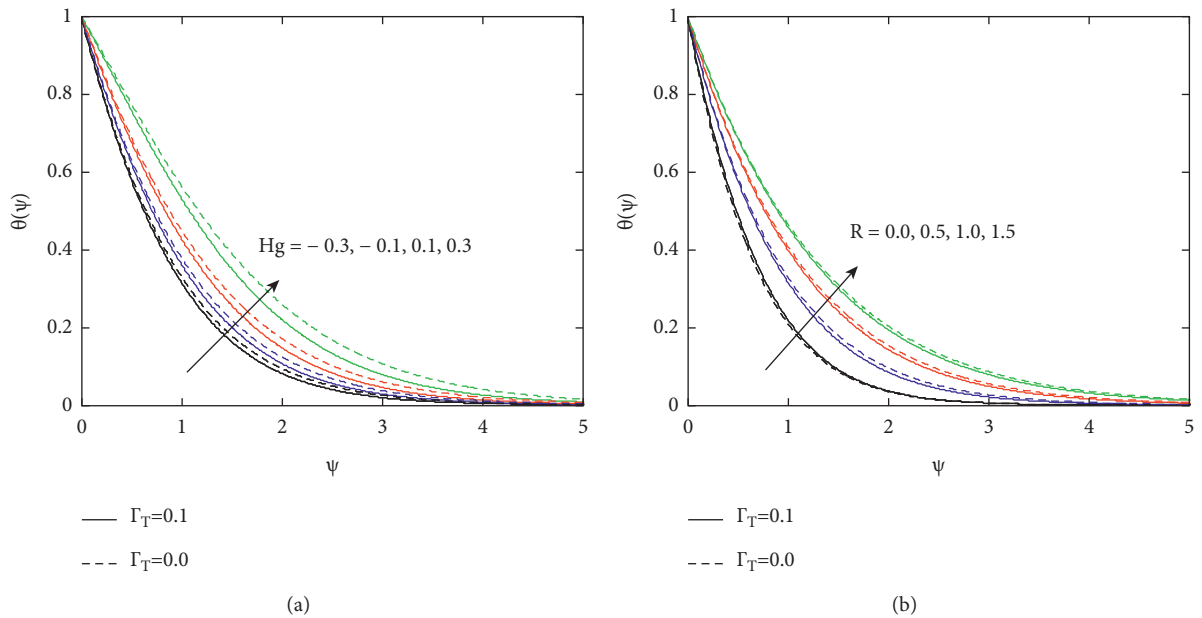


FIGURE 6: The temperature distribution for diverse quantity of Hg (a) and R (b).

heat transfer gradient (3.2986) occurs in heat-absorbing nonradiative viscous nanofluid, and a smaller heat transfer gradient (0.646887) occurs in heat-generating radiative Williamson nanofluid. Figures 13(a) and 13(b) provide the local Sherwood number on various

combinations of E and n of a CC, FF flow of WNF and VNF. The larger mass transfer gradient (-1.0171) occurs in FF without activation energy, and a smaller mass transfer gradient (-1.03809) occurs in the CC model with $n = -0.5$.

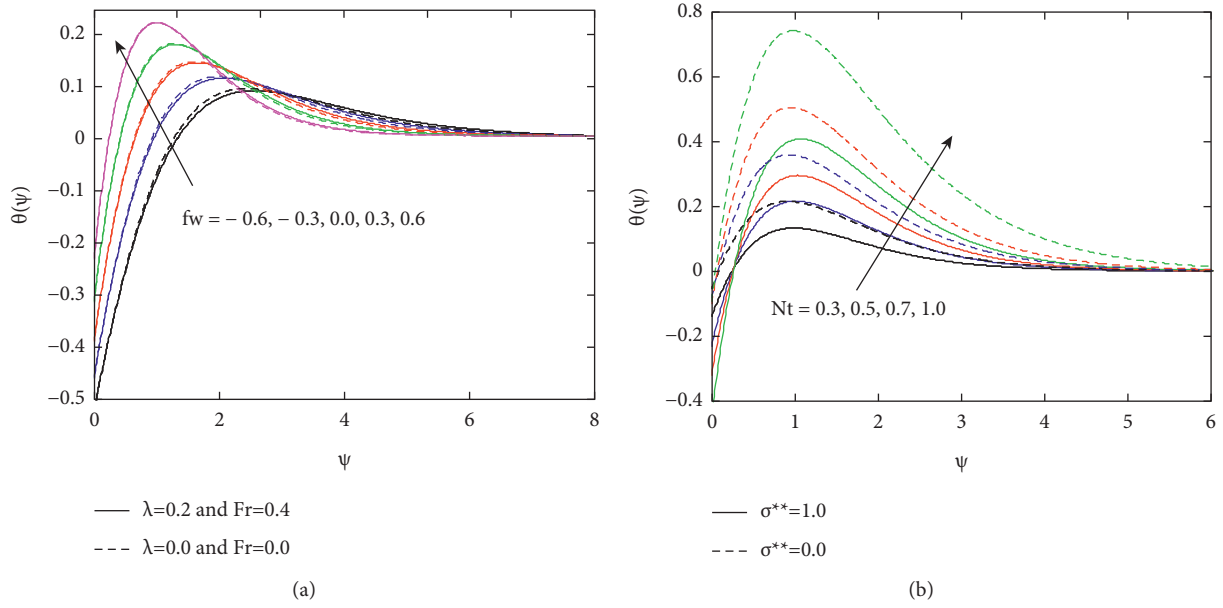


FIGURE 7: The nanofluid concentration distribution for diverse quantity of fw (a) and Nt (b).

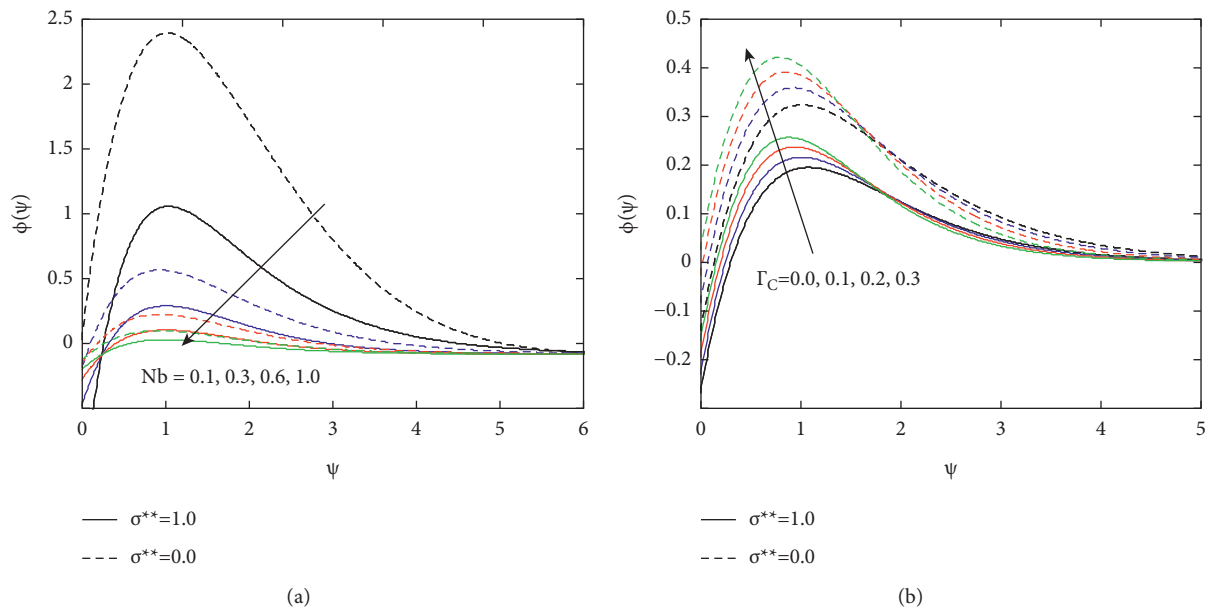


FIGURE 8: The nanofluid concentration distribution for diverse quantity of Nb (a) and Γ_C (b).

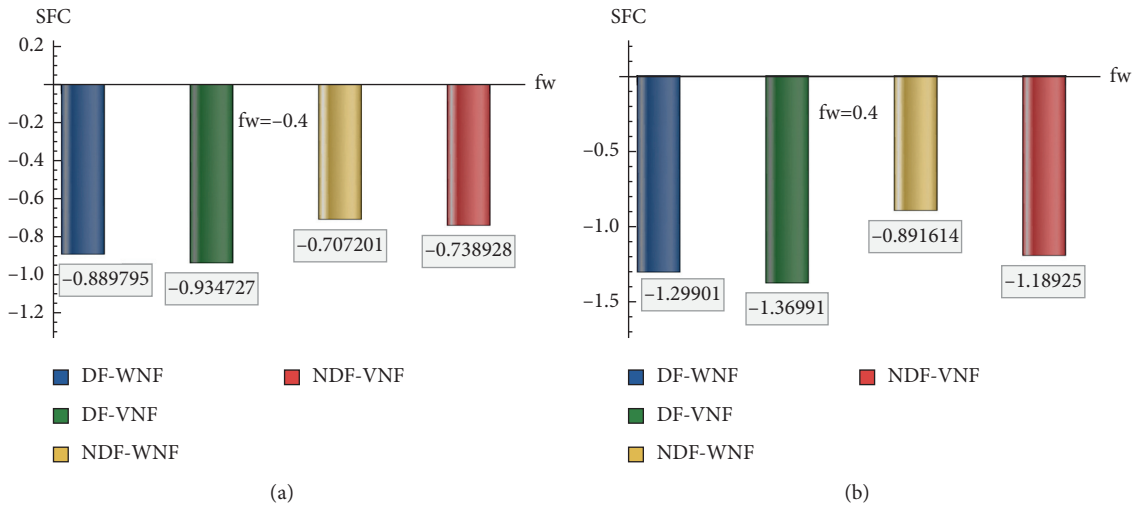


FIGURE 9: The skin friction coefficient on WNF and VNF on a DFPM and NDFPM with $fw = -0.4$ (a) and $fw = 0.4$ (b).

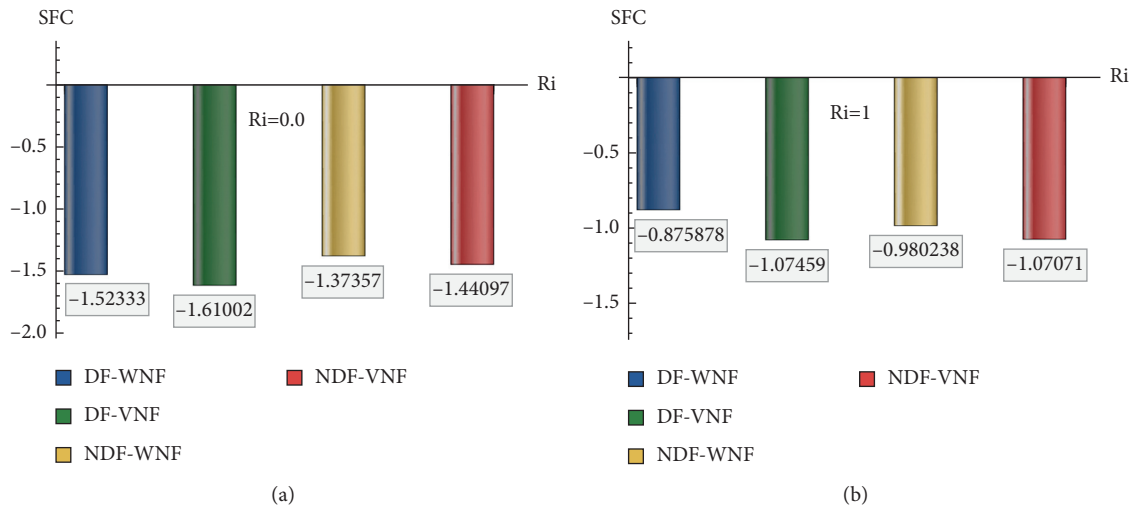


FIGURE 10: The skin friction coefficient on WNF and VNF on a DFPM and NDFPM with $Ri = 0.0$ (a) and $Ri = 1.0$ (b).

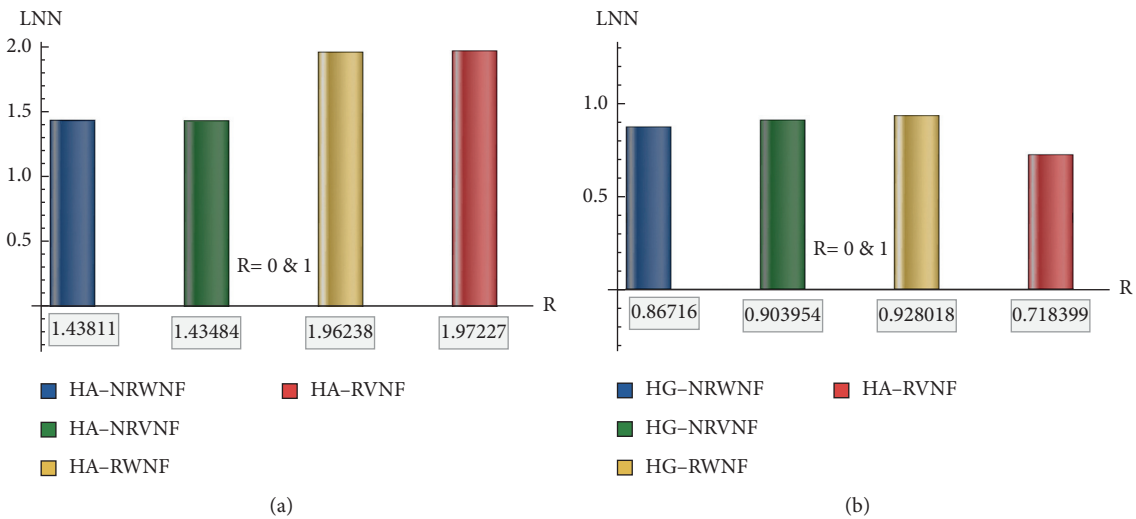


FIGURE 11: The local Nusselt number on various combinations of Hg and R of a CCHF flow of WNF and VNF.

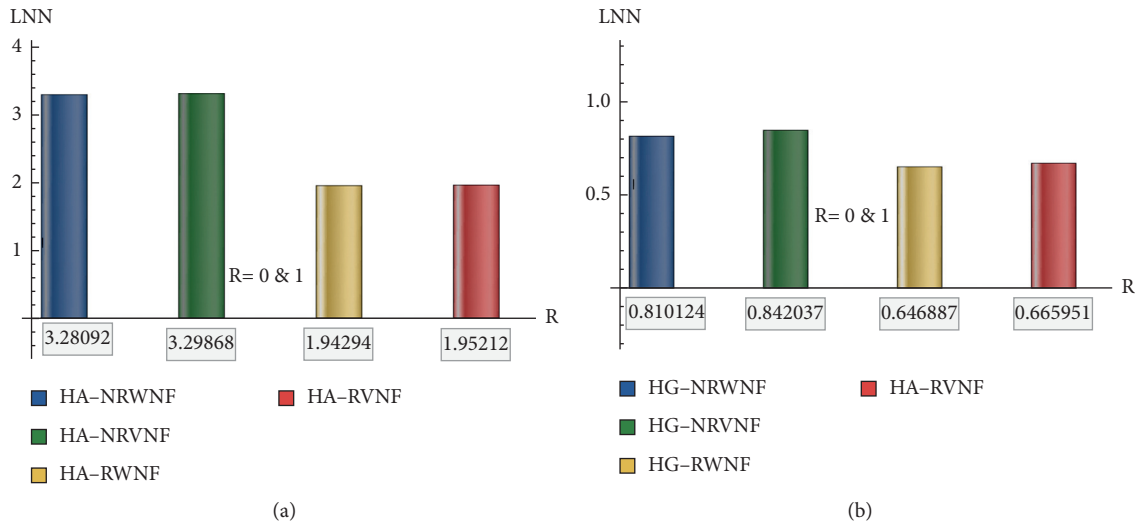


FIGURE 12: The local Nusselt number on various combinations of Hg and R of a FHF flow of WNF and VNF.

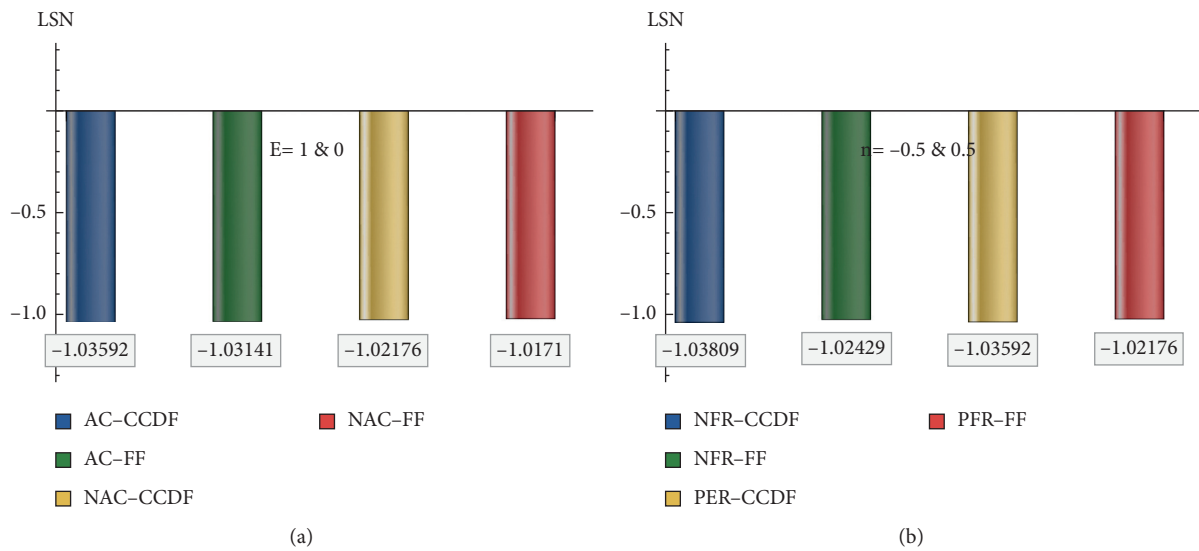


FIGURE 13: The local Sherwood number on various combinations of E and n of a CCMF and FMF flow of WNF and VNF.

5. Conclusions

This analysis clearly shows the consequences of thermal radiation of a Darcy–Forchheimer flow of Williamson nanofluid on a stretchy plate with a magnetic field. The energy and nanoparticle concentration equations were framed with Cattaneo–Christov heat-mass flux theory. Additionally, the mass transfer analysis is made by activation energy and binary chemical reaction. The governing PDE problems were converted into ODE problems by applying suitable variables, and these equations were solved using MATLAB bvp4c algorithm. The salient outcomes of the current analysis are outlined as below:

(i) The fluid velocity decelerates when enhancing the Williamson fluid, magnetic field, and porosity

parameters, and it accelerates by increasing the Richardson number.

- (ii) The fluid temperature accelerates when strengthening the heat generation/absorption radiation and thermophoresis parameters, and it declines when increasing the Brownian motion parameter.
- (iii) The fluid concentration suppresses when increasing the Brownian motion parameter, and it enhances when escalating the thermophoresis and mass relaxation time parameters.
- (iv) The smaller SFC occurs in the non-Darcy–Forchheimer flow of Williamson nanofluid.
- (v) The larger heat transfer gradient exists in viscous nanofluid without radiation.

- (vi) The larger Sherwood number attains in the Fourier mass flux model without activation energy.

The skin friction coefficient on WNF and VNF on a DFPM and NDFPM with $Ri = 0.0$ and $Ri = 1.0$ was plotted in Figures.

Nomenclature

a :	Constant
B_0 :	Magnetic field strength
C :	Fluid concentration
C_b :	Drag coefficient
C_p :	Specific heat ($\text{Jkg}^{-1}\text{K}^{-1}$)
C_w :	Wall concentration
C_∞ :	Ambient fluid concentration
D_B :	Mass diffusivity
D_T :	Thermophoretic diffusion coefficient
$E = (E_a/\kappa T_\infty)$:	Nondimensional activation energy
E_a :	Activation energy
$Fr = (C_b/\sqrt{k_2})$:	Forchheimer number
f' :	Nondimensional velocity
$fw = (V_w/\sqrt{a\nu})$:	Suction/injection parameter
g :	Acceleration due to gravity
$Gr_x = ((g\beta(1 - C_\infty)(T_w - T_\infty)x^3)/\nu^2)$:	Local Grashof number
$Hg = (Q/\rho_f C_p a)$:	Heat generation/absorption parameter
k :	Thermal conductive
k_1 :	Permeability of porous medium
k^* :	Mean absorption coefficient
k_r :	Reaction rate
$M = (\sigma B_0^2/\rho_f a)$:	Hartmann number
n :	Fitted rate
$Nb = (\tau D_B C_\infty/\nu)$:	Brownian diffusion parameter
$Nr = ((\rho_p - \rho_{f_\infty})C_\infty/(\rho_{f_\infty}\beta(1 - C_\infty)(T_w - T_\infty)))$:	Buoyancy ratio parameter
$Nt = (\tau D_T (T_w - T_\infty)/T_\infty \nu)$:	Thermophoresis parameter
$Pr = (\nu/\alpha)$:	Prandtl number
Q :	Heat generation/absorption coefficient
$R = (4\sigma^* T_\infty^3/kk^*)$:	Thermal radiation
$Re_x = (U_w x/\nu)$:	Local Reynolds number
$Ri = (Gr_x/Re_x^2 = (g\beta(1 - C_\infty)(T_w - T_\infty)/a^2 x))$:	Richardson number
$Sc = (\nu/D_B)$:	Schmith number
T :	Fluid temperature (K)
T_∞ :	Ambient temperature (K)
T_w :	Wall temperature (K)
u and v :	Velocity components (ms^{-1})
U_w :	Stretching surface velocity (ms^{-1})
$We = (\Gamma x \sqrt{2a^3/\nu})$:	Weissenberg number
x and y :	Direction coordinates (m)

Greek symbols

α :	Thermal diffusivity ($\text{m}^2 \text{s}^{-1}$)
β :	Thermal expansion coefficient

$\delta = ((T_w - T_\infty)/T_\infty)$:	Temperature difference parameter
Γ :	Williamson parameter
$\Gamma_T = (a\lambda_T)$:	Thermal relaxation parameter
$\Gamma_C = (a\lambda_C)$:	Solute relaxation parameter
$\lambda = (\nu/k_2 a)$:	Local porosity parameter
λ_C :	Relaxation time of mass flux
λ_T :	Relaxation time of heat flux
ν :	Kinematic viscosity (m^2s^{-1})
ϕ :	Nondimensional nanofluid concentration
ρ_f :	Fluid density (kgm^{-3})
σ :	Electrical conductivity
σ^* :	Stefan Boltzmann constant ($\text{Wm}^{-2}\text{K}^{-4}$)
$\sigma^{**} = (k_r^2/a)$:	Dimensionless reaction rate
τ :	The ratio of effective heat capacity of the nanoparticle material and heat capacity of the fluid
θ :	Nondimensional temperature

Abbreviations

AC:	Activation energy
CCHF:	Cattaneo – Christov heat flux
DF (F):	Darcy – Forchheimer (flow)
FHF:	Fourier heat flux model
HA:	Heat absorption
HG:	Heat generation
NAC:	Nonactivation energy
NDF (F):	Non – Darcy – Forchheimer (flow)
NDFPM:	Non – Darcy – Forchheimer porous medium
NFR:	Negative fitted rate
NRVNF:	Nonradiative viscous nanofluid
NRWNF:	Nonradiative Williamson nanofluid
PFR:	Positive fitted rate
RVNF:	Radiative viscous nanofluid
RWNF:	Radiative Williamson nanofluid
VNF:	Viscous nanofluid
WNF:	Williamson nanofluid.

Data Availability

The data used to support the findings of the study are available from the corresponding author upon request.

Conflicts of Interest

The authors declare that they have no conflicts of interest.

Authors' Contributions

All authors contributed equally to this work. All the authors have read and approved the final version manuscript.

Acknowledgments

This research was funded by the Deanship of Scientific Research at Princess Nourah Bint Abdulrahman University through the Fast-Track Research Funding Program.

References

- [1] W. A. Khan and I. Pop, "Boundary-layer flow of a nanofluid past a stretching sheet," *International Journal of Heat and Mass Transfer*, vol. 53, no. 11-12, pp. 2477–2483, 2010.
- [2] A. V. Kuznetsov and D. A. Nield, "Natural convective boundary-layer flow of a nanofluid past a vertical plate," *International Journal of Thermal Sciences*, vol. 49, no. 2, pp. 243–247, 2010.
- [3] M. Goyal and R. Bhargava, "Boundary layer flow and heat transfer of viscoelastic nanofluids past a stretching sheet with partial slip conditions," *Applied Nanoscience*, vol. 4, no. 6, pp. 761–767, 2014.
- [4] F. Mebarek-Oudina, "Convective heat transfer of titania nanofluids of different base fluids in cylindrical annulus with discrete heat source," *Heat Transfer—Asian Research*, vol. 48, no. 1, pp. 135–147, 2019.
- [5] A. Shafiq, Z. Hammouch, and T. N. Sindhu, "Bioconvective MHD flow of tangent hyperbolic nanofluid with Newtonian heating," *International Journal of Mechanical Sciences*, vol. 133, pp. 759–766, 2017.
- [6] F. Mabood, A. Shafiq, W. A. Khan, and I. A. Badruddin, "MHD and nonlinear thermal radiation effects on hybrid nanofluid past a wedge with heat source and entropy generation," *International Journal of Numerical Methods for Heat and Fluid Flow*, 2021, In press.
- [7] C. Cattaneo, "Sulla conduzione del calore," *Atti del Seminario Matematico e Fisico dell'Universita di Modena e Reggio Emilia*, vol. 3, pp. 83–101, 1948.
- [8] C. I. Christov, "On frame indifferent formulation of the Maxwell-Cattaneo model of finite-speed heat conduction," *Mechanics Research Communications*, vol. 36, no. 4, pp. 481–486, 2009.
- [9] I. Ahmad, M. Faisal, T. Javed, and I. L. Animasaun, "Insight into the relationship between unsteady Cattaneo-Christov double diffusion, random motion and thermo-migration of tiny particles," *Ain Shams Engineering Journal*, 2021, In press.
- [10] M. G. Reddy and K. G. Kumar, "Cattaneo-Christov heat flux feature on carbon nanotubes filled with micropolar liquid over a melting surface: a stream line study," *International Communications in Heat and Mass Transfer*, vol. 122, Article ID 105142, 2021.
- [11] W. Ibrahim and G. Gadisa, "Finite element solution of nonlinear convective flow of Oldroyd-B fluid with Cattaneo-Christov heat flux model over nonlinear stretching sheet with heat generation or absorption," *Propulsion and Power Research*, vol. 9, no. 3, pp. 304–315, 2020.
- [12] K. A. Kumar, J. V. Ramana Reddy, V. Sugunamma, and N. Sandeep, "Magnetohydrodynamic Cattaneo-Christov flow past a cone and a wedge with variable heat source/sink," *Alexandria Engineering Journal*, vol. 57, no. 1, pp. 435–443, 2018.
- [13] S. Han, L. Zheng, C. Li, and X. Zhang, "Coupled flow and heat transfer in viscoelastic fluid with Cattaneo-Christov heat flux model," *Applied Mathematics Letters*, vol. 38, pp. 87–93, 2014.
- [14] G. K. Ramesh, B. J. Gireesha, S. A. Shehzad, and F. M. Abbasi, "Analysis of heat transfer phenomenon in magnetohydrodynamic Casson fluid flow through cattaneo-christov heat diffusion theory," *Communications in Theoretical Physics*, vol. 68, no. 1, pp. 91–92, 2017.
- [15] S. A. M. Haddad, "Thermal instability in Brinkman porous media with Cattaneo-Christov heat flux," *International Journal of Heat and Mass Transfer*, vol. 68, pp. 659–668, 2014.
- [16] O. D. Makinde, S. Eswaramoorthi, M. Bhuvanewari, and S. Sivasankaran, "Heterogeneous and homogeneous reaction analysis on MHD Oldroyd-B fluid with cattaneo-christov heat flux model and convective heating," *Defect and Diffusion Forum*, vol. 387, pp. 194–206, 2018.
- [17] F. O. M. Mallawi, M. Bhuvanewari, S. Sivasankaran, and S. Eswaramoorthi, "Impact of double-stratification on convective flow of a non-Newtonian liquid in a Riga plate with Cattaneo-Christov double-flux and thermal radiation," *Ain Shams Engineering Journal*, vol. 12, no. 1, pp. 969–981, 2021.
- [18] K. Loganathan, N. Alessa, N. Namgyel, and T. S. Karthik, "MHD flow of thermally radiative Maxwell fluid past a heated stretching sheet with Cattaneo-Christov dual diffusion," *Journal of Mathematics*, vol. 2021, Article ID 5562667, 10 pages, 2021.
- [19] Y. Zhang, B. Yuan, Y. Bai, Y. Cao, and Y. Shen, "Unsteady Cattaneo-Christov double diffusion of Oldroyd-B fluid thin film with relaxation-retardation viscous dissipation and relaxation chemical reaction," *Powder Technology*, vol. 338, pp. 975–982, 2018.
- [20] P. Forchheimer, "Wasserbewegung durch boden," *Zeitschrift des Vereins deutscher Ingenieure*, vol. 45, pp. 1782–1788, 1901.
- [21] D. Pal and H. Mondal, "Hydromagnetic convective diffusion of species in Darcy-Forchheimer porous medium with non-uniform heat source/sink and variable viscosity," *International Communications in Heat and Mass Transfer*, vol. 39, no. 7, pp. 913–917, 2012.
- [22] S. A. Bakar, N. M. Arifin, R. Nazar, F. M. Ali, and I. Pop, "Forced convection boundary layer stagnation-point flow in Darcy-Forchheimer porous medium past a shrinking sheet," *Frontiers in Heat and Mass Transfer*, vol. 7, no. 38, pp. 1–6, 2016.
- [23] M. A. Meraj, S. A. Shehzad, T. Hayat, F. M. Abbasi, and A. Alsaedi, "Darcy-Forchheimer flow of variable conductivity Jeffrey liquid with Cattaneo-Christov heat flux theory," *Applied Mathematics and Mechanics*, vol. 38, no. 4, pp. 557–566, 2017.
- [24] T. Hayat, F. Haider, T. Muhammad, and A. Alsaedi, "On Darcy-Forchheimer flow of carbon nanotubes due to a rotating disk," *International Journal of Heat and Mass Transfer*, vol. 112, pp. 248–254, 2017.
- [25] G. Rasool, A. Shafiq, C. M. Khaliq, and T. Zhang, "Magnetohydrodynamic Darcy-Forchheimer nanofluid flow over a nonlinear stretching sheet," *Physica Scripta*, vol. 94, no. 10, Article ID 105221, 2019.
- [26] A. S. Alshomrani and M. Z. Ullah, "Effects of homogeneous-heterogeneous reactions and convective condition in Darcy-Forchheimer flow of carbon nanotubes," *Journal of Heat Transfer*, vol. 141, Article ID 012405, 2019.
- [27] G. Rasool, T. Zhang, A. J. Chamkha, A. Shafiq, I. Tlili, and G. Shahzadi, "Entropy generation and consequences of binary chemical reaction on MHD Darcy-Forchheimer Williamson nanofluid flow over non-linearly stretching surface," *Entropy*, vol. 22, no. 1, pp. 1–12, 2019.
- [28] G. Rasool, A. J. Chamkha, T. Muhammad, A. Shafiq, and I. Khan, "Darcy-Forchheimer relation in Casson type MHD nanofluid flow over non-linear stretching surface," *Propulsion and Power Research*, vol. 9, no. 2, pp. 159–168, 2020.
- [29] R. S. Saif, T. Muhammad, and H. Sadia, "Significance of inclined magnetic field in Darcy-Forchheimer flow with variable porosity and thermal conductivity," *Physica A: Statistical Mechanics and Its Applications*, vol. 551, Article ID 124067, 2020.

- [30] M. N. Khan and S. Nadeem, "Consequences of Darcy-Forchheimer and Cattaneo-Christov on a radiative three-dimensional Maxwell fluid flow over a vertical surface," *Journal of the Taiwan Institute of Chemical Engineers*, vol. 118, pp. 1–11, 2021.
- [31] M. I. Khan, "Transportation of hybrid nanoparticles in forced convective Darcy-Forchheimer flow by a rotating disk," *International Communications in Heat and Mass Transfer*, vol. 122, Article ID 105177, 2021.
- [32] K. Loganathan, N. Alessa, K. Tamilvanan, and F. S. Alshammari, "Significances of Darcy-Forchheimer porous medium in third-grade nanofluid flow with entropy features," *The European Physical Journal—Special Topics*, vol. 230, no. 5, pp. 1293–1305, 2021.
- [33] F. O. M. Mallawi, S. Eswaramoorthi, S. Sivasankaran, and M. Bhuvaneswari, "Impact of stratifications and chemical reaction on convection of a non-Newtonian fluid in a Riga plate with thermal radiation and Cattaneo-Christov flux," *Journal of Thermal Analysis and Calorimetry*, 2021, In press.
- [34] F. O. M. Mallawi, S. Eswaramoorthi, M. Bhuvaneswari, and S. Sivasankaran, "Impact of double-diffusion and slip of order 2 on convection of chemically reacting Oldroyd-B liquid with Cattaneo-Christov dual flux," *Thermal Science*, In press, 2021.
- [35] Y.-Q. Song, S. Ali Khan, M. Imran et al., "Applications of modified Darcy law and nonlinear thermal radiation in bioconvection flow of micropolar nanofluid over an off centered rotating disk," *Alexandria Engineering Journal*, vol. 60, no. 5, pp. 4607–4618, 2021.
- [36] M. Javed, A. A. Alderremy, M. Farooq, A. Anjum, S. Ahmad, and M. Y. Malik, "Analysis of activation energy and melting heat transfer in MHD flow with chemical reaction," *The European Physical Journal Plus*, vol. 134, no. 6, Article ID 256, 2019.
- [37] A. Zaib, M. M. Rashidi, A. J. Chamkha, and A. F. Al-Mudhaf, "Nonlinear radiation effect on Casson nanofluid past a plate immersed in Darcy-Brinkman porous medium with binary chemical reaction and activation energy," *International Journal of Fluid Mechanics Research*, vol. 44, no. 6, pp. 513–531, 2017.
- [38] K.-L. Hsiao, "To promote radiation electrical MHD activation energy thermal extrusion manufacturing system efficiency by using Carreau-Nanofluid with parameters control method," *Energy*, vol. 130, pp. 486–499, 2017.
- [39] K. M. Maleque, "Effects of exothermic/endothemic chemical reactions with Arrhenius activation energy on MHD free convection and mass transfer flow in presence of thermal radiation," *Journal of Thermodynamics*, vol. 2013, Article ID 692516, 11 pages, 2013.
- [40] F. Mabood, M. K. Nayak, and A. J. Chamkha, "Heat transfer on the cross flow of micropolar fluids over a thin needle moving in a parallel stream influenced by binary chemical reaction and Arrhenius activation energy," *The European Physical Journal Plus*, vol. 134, no. 9, Article ID 427, 2019.
- [41] K. G. Kumar, A. Baslem, B. C. Prasannakumara, J. Majdoubi, M. Rahimi-Gorji, and S. Nadeem, "Significance of Arrhenius activation energy in flow and heat transfer of tangent hyperbolic fluid with zero mass flux condition," *Microsystem Technologies*, vol. 26, no. 8, pp. 2517–2526, 2020.
- [42] M. I. Khan, M. W. A. Khan, A. Alsaedi, T. Hayat, and M. I. Khan, "Entropy generation optimization in flow of non-Newtonian nanomaterial with binary chemical reaction and Arrhenius activation energy," *Physica A: Statistical Mechanics and Its Applications*, vol. 538, Article ID 122806, 2020.
- [43] M. I. Khan, S. Qayyum, T. Hayat, M. Waqas, M. I. Khan, and A. Alsaedi, "Entropy generation minimization and binary chemical reaction with Arrhenius activation energy in MHD radiative flow of nanomaterial," *Journal of Molecular Liquids*, vol. 259, pp. 274–283, 2018.
- [44] F. Mallawi and M. Z. Ullah, "Conductivity and energy change in Carreau nanofluid flow along with magnetic dipole and Darcy-Forchheimer relation," *Alexandria Engineering Journal*, vol. 60, no. 4, pp. 3565–3575, 2021.
- [45] M. I. Khan, T. Hayat, M. I. Khan, and A. Alsaedi, "Activation energy impact in nonlinear radiative stagnation point flow of Cross nanofluid," *International Communications in Heat and Mass Transfer*, vol. 91, pp. 216–224, 2018.
- [46] M. Kothandapani and J. Prakash, "Effects of thermal radiation parameter and magnetic field on the peristaltic motion of Williamson nanofluids in a tapered asymmetric channel," *International Journal of Heat and Mass Transfer*, vol. 81, pp. 234–245, 2015.
- [47] M. Mustafa, J. A. Khan, T. Hayat, and A. Alsaedi, "Buoyancy effects on the MHD nanofluid flow past a vertical surface with chemical reaction and activation energy," *International Journal of Heat and Mass Transfer*, vol. 108, pp. 1340–1346, 2017.